PHYSICAL REVIEW B **96**, 205204 (2017)

Population decay time and distribution of exciton states analyzed by rate equations based on theoretical phononic and electron-collisional rate coefficients

Kensuke Oki,[*] Bei Ma, and Yoshihiro Ishitani[†]
Department of Electrical and Electronic Engineering, Chiba University, 1-33 Yayoicho, Inage-ku, Chiba 263-8522, Japan

(Received 10 August 2017; revised manuscript received 27 October 2017; published 21 November 2017)

Population distributions and transition fluxes of the *A* exciton in bulk GaN are theoretically analyzed using rate equations of states of the principal quantum number *n* up to 5 and the continuum. These rate equations consist of the terms of radiative, electron-collisional, and phononic processes. The dependence of the rate coefficients on temperature is revealed on the basis of the collisional-radiative model of hydrogen plasma for the electron-collisional processes and theoretical formulation using Fermi's "golden rule" for the phononic processes. The respective effects of the variations in electron, exciton, and lattice temperatures are exhibited. This analysis is a base of the discussion on nonthermal equilibrium states of carrier-exciton-phonon dynamics. It is found that the exciton dissociation is enhanced even below 150 K mainly by the increase in the lattice temperature. When the thermal-equilibrium temperature increases, the population fluxes between the states of $n > 1$ and the continuum become more dominant. Below 20 K, the severe deviation from the Saha-Boltzmann distribution occurs owing to the interband excitation flux being higher than the excitation flux from the $1S$ state. The population decay time of the $1S$ state at 300 K is more than ten times longer than the recombination lifetime of excitons with kinetic energy but without the upper levels ($n > 1$ and the continuum). This phenomenon is caused by a shift of population distribution to the upper levels. This phonon-exciton-radiation model gives insights into the limitations of conventional analyses such as the ABC model, the Arrhenius plot, the two-level model ($n = 1$ and the continuum), and the neglect of the upper levels.

DOI: 10.1103/PhysRevB.96.205204

I. INTRODUCTION

Wannier excitons in semiconductors have higher radiative recombination rates than free carriers, and dominate optical properties at temperatures below a few tens of Kelvin. In wide-band-gap materials such as GaN, AlN, and ZnO, the exciton binding energies are tens of meV, and the luminescence spectra reflect the excitonic recombination processes even at room temperature [1–3]. In contrast, the lasing from exciton-exciton scattering in GaN has not been observed above 150 K [4]. This phenomenon is considered to be due to the Mott transition. However, it is unclear why the free-carrier density exceeds the Mott density before the lasing of excitons occurs. The exciton dissociation is possibly enhanced by the nonthermal equilibrium state for the different effective temperatures of carriers, excitons, and lattice. The nonthermal equilibrium state of excitons has been studied in many works [5–10]. In Ref. [6], it takes 150 ps for the exciton temperature to decrease from approximately 110 K to the sample temperature of 20 K.

The recombination probability of free excitons is important for the optical properties [11–22]. However, the radiative recombination probability is only partly understood both experimentally and theoretically [11,12,23]. The inverse of the radiative recombination probability of $1S$ excitons in bulk GaN is theoretically calculated to be 0.34 to 3.8 ns for 60 to 300 K in Ref. [24], but is experimentally estimated to be 3 to 17 ns in Ref. [25]. As in Ref. [25], the decay time of $1S$-exciton luminescence has been often considered to be approximately equal to the inverse of the recombination probability. However, $1S$ exciton population is supplied from the upper levels such as the free carrier and the excitons with principal quantum number $n \geqslant 2$, which possibly makes the decay time longer than the inverse of the recombination probability. In Ref. [26], the recombination probability is estimated by assuming the Saha equation and taking into account the transition between $1S$ excitons and free carriers. Although this estimation neglected the excitons with $n \geqslant 2$, the $1S$-exciton density possibly varies owing to excitation and deexcitation related to $n \geqslant 2$. Thus, the population densities of the excitons with $n \geqslant 1$ and free carriers are required for a more rigorous estimation of the recombination probability.

Free-carrier dynamics has been often studied using the ABC model [27–30]. However, below the Mott density, this model is insufficient because the exciton population has to be taken into account [31]. The dynamics of excitons and free carriers has been investigated using the rate equation of each level (such as free excitons, bound excitons, and free carriers) [15,16,19,26,31–38]. However, the determination of the rate coefficients for transitions among these levels has been considered to be "a formidable challenge for both experiment and theory" [33]. One experimental piece of data has been fitted by several free parameters including the rate coefficients. The rate equations have also been simplified by assumptions such as the common decay time of all levels [33], the neglect of the free-carrier level [38], and the Saha equation [19,26]. These fitting and assumptions probably reduce the accuracy of the parameters obtained by the rate equations.

In addition, there are only a few investigations by the rate equations including the excitons of $n \geqslant 2$. Recently, an effective exciton temperature of $n = 2$ has been observed to have a longer relaxation time than $n = 1$ in GaN [39]. This result indicates the strong coupling between the state of $n = 2$ and the continuum. The states of $n \geqslant 2$ probably affect the dynamics of free carriers and $1S$ excitons. Although the states

---

[*] okiken@chiba-u.jp

[†] ishitani@faculty.chiba-u.jp

2469-9950/2017/96(20)/205204(15)

of $n \geqslant 3$ have not been observed in discrete optical spectra of GaN, these states are presumed to exist as in other materials (e.g., see Refs. [40–42]) and be included in continuous spectra near the band edge. It is probably difficult to include the effects of the states of $n \geqslant 3$ in experimental analyses, and thus these effects should be theoretically investigated.

In this paper, the rate coefficients among free carriers and free excitons with n up to 5 in bulk GaN are theoretically calculated in order to develop a more rigorous model for the densities of free carriers and excitons. The radiative and electron-collisional rate coefficients are calculated using the formulas of the collisional-radiative (CR) model for hydrogen plasma [43,44]. The rate coefficients for phonon emission and absorption are calculated by the integration of Fermi's "golden rule" with the Maxwellian velocity distribution and the Bose-Einstein distribution, where the matrix elements for n up to 5 are rigorously calculated. We show the dependence of these rate coefficients on the effective temperatures of electrons (T_e), excitons (T_X), and lattice (T_L), separately. From these calculations, a phonon-exciton-radiation (PXR) model is constructed.

The population densities in the steady state are calculated by solving the rate equations. Dependence of the population densities on the interband excitation rate and the temperatures is presented. The effects of the nonthermal equilibrium on the exciton dissociation are shown. The population densities calculated using the rate equations are compared with those obtained by the Saha-Boltzmann distribution, which is related to the thermal and nonthermal regimes. The Saha-Boltzmann distribution has been utilized in studies on the dynamics of excitons and free carriers [19,26,32,36,45]. In Ref. [26], the Saha equation is utilized for the estimation of the recombination probability as mentioned above. It is important to verify the validity of the Saha-Boltzmann distribution.

The time evolution of the population densities is also calculated using the rate equations. For various temperatures and densities, we quantitatively reveal the difference between the $1S$-exciton decay time and the recombination probability.

II. RATE EQUATIONS

The rate equations for exciton density $N_X(n)$ are

$$\frac{d}{dt}N_X(n) = \Gamma_{\text{in}}(n) - \Gamma_{\text{out}}(n), \tag{1a}$$

$$\begin{aligned}\Gamma_{\text{in}}(n) = &\sum_{n'\neq n}[A(n',n) + C(n',n)N_e + W_{XX}(n',n)]N_X(n') \\ &+ [\beta(n) + \alpha(n)N_e + W_{CX}(n)]N_eN_h + R_{VX}(n),\end{aligned} \tag{1b}$$

$$\begin{aligned}\Gamma_{\text{out}}(n) = &\left\{\sum_{n'\neq n}[A(n,n') + C(n,n')N_e + W_{XX}(n,n')]\right. \\ &\left. + S(n)N_e + W_{XC}(n) + P_{\text{rec}}(n)\right\}N_X(n),\end{aligned} \tag{1c}$$

where $\Gamma_{\text{in}}(n)$ and $\Gamma_{\text{out}}(n)$ are population influx and outflux, respectively, for the state of n. N_e and N_h are densities of free electrons and holes, respectively. $A(n,n')$, $C(n,n')$, and $W_{XX}(n,n')$ are the rate coefficients of transitions from n to n' by radiative, electron-collisional, and phononic processes, respectively. $\beta(n)$, $\alpha(n)$, and $W_{CX}(n)$ are the exciton-formation rate coefficients of radiative, electron-collisional, and phononic processes, respectively. $S(n)$ and $W_{XC}(n)$ are the exciton-dissociation rate coefficients of electron-collisional and phononic processes, respectively. $P_{\text{rec}}(n)$ is the recombination probability of excitons in the state of n. $R_{VX}(n)$ is the excitation rate of excitons from the vacuum state (electrons in the valence band) to the state of n. As in the hydrogen plasma model [43,44], $N_X(n,l,m) = N_X(n)/n^2$ is assumed, where $N_X(n,l,m)$ denotes the exciton density for the azimuthal quantum number l and the magnetic quantum number m. The rate equation for N_e is

$$\frac{d}{dt}N_e = \Gamma^e_{\text{in}} - \Gamma^e_{\text{out}}, \tag{2a}$$

$$\Gamma^e_{\text{in}} = \sum_n [S(n)N_e + W_{XC}(n)]N_X(n) + R_{VC}, \tag{2b}$$

$$\Gamma^e_{\text{out}} = \sum_n [\beta(n) + \alpha(n)N_e + W_{CX}(n)]N_eN_h, \tag{2c}$$

where Γ^e_{in} and Γ^e_{out} are electron-population influx and outflux, respectively. R_{VC} is the excitation rate from the vacuum state to the continuum state (electrons in the conduction band). Figure 1 shows a schematic diagram of the energy levels and transition processes included in the rate equations.

In this paper, the levels of crystal defects and impurities are excluded. The charge neutrality condition $N_e = N_h$ is assumed. The parameters used in our calculation are listed in Table I. The Maxwellian velocity distribution is assumed for free carriers and excitons. The Bose-Einstein distribution is assumed for phonons. The hole effective temperature is assumed to be equal to T_e. The temperatures of T_e, T_X, and T_L are varied within a range from 10 to 300 K. $N_X(n)$ and N_e are lower than the Mott density for $n = 5$, which is $N_M(5) = 3.6\times10^{17}\text{cm}^{-3}$. This Mott density is estimated from $N_M(5) = 1/(5a_X)^3$, where a_X is the $1S$-exciton Bohr radius. Our model excludes the exciton-exciton scattering, the biexciton processes, and the recombination of free electrons and holes. A theoretical study showed that the rate coefficient B of the recombination of free electrons and holes is approximately proportional to $T_e^{-3/2}$, and is 0.47×10^{-10} cm^3 s^{-1} at 300 K [24]. Thus, B is possibly lower than 8×10^{-9} cm^3 s^{-1} in the range from 10 to 300 K. This value is much lower than $W_{CX}(n) > 3\times10^{-6}$ cm^3 s^{-1} presented in Sec. III B.

Although GaN has the anisotropic wurtzite structure, the isotropic system is assumed for our calculations.

III. RATE COEFFICIENTS

A. Radiative and electron-collisional rate coefficients based on the hydrogen plasma model

The radiative rate coefficients $A(n,n')$ and $\beta(n)$ and the electron-collisional rate coefficients $C(n,n')$, $S(n)$, and $\alpha(n)$ are calculated using the CR model for hydrogen plasma [43,44]. The electron rest mass m_0 and the vacuum dielectric constant ϵ_0 in the formulas for hydrogen plasma are replaced

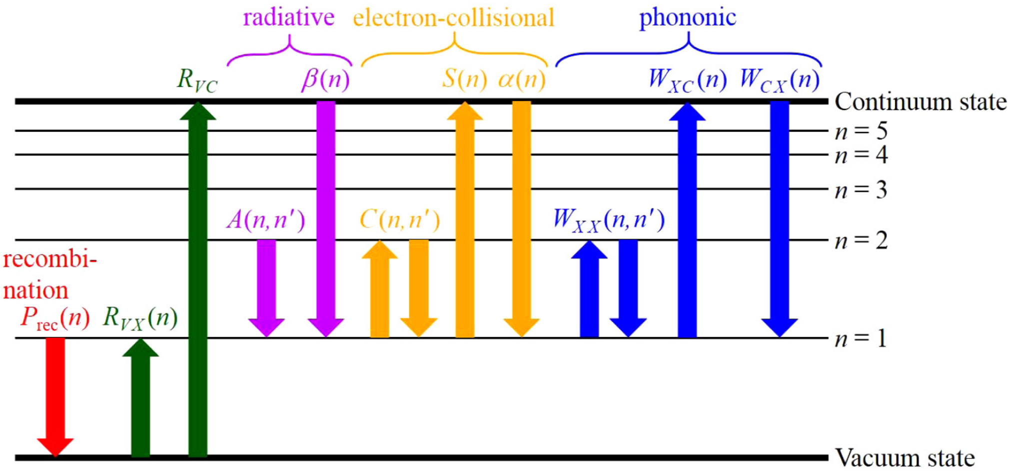

FIG. 1. Schematic diagram of the energy levels and transition processes (arrows) included in the rate equations. The rate coefficients are displayed above the arrows.

with the electron effective mass m_e and the static dielectric constant ϵ_s of GaN, respectively. The exciton Bohr radius a_X and the exciton binding energy $E_B(n) = E_B(1)/n^2$ are calculated using ϵ_s and the exciton effective reduced mass $\mu = (m_e^{-1} + m_h^{-1})^{-1}$, where m_h is the hole effective mass. The relative velocity of electrons to excitons is assumed to be equal to the absolute velocity of electrons, as in the CR model, because the A exciton effective mass $M = m_e + m_h = 1.96m_0$ is approximately ten times greater than $m_e = 0.20m_0$.

The radiative deexcitation rate coefficient $A(n,n')$ for $n > n'$ is

$$A(n,n') = \frac{2\pi e_0^2[E(n,n')]^2}{h^2\mu c_0^3\epsilon_s}\frac{g(n')}{g(n)}f_{n',n}, \tag{3}$$

where e_0 is the elementary charge, $E(n,n')$ is $|E_B(n) - E_B(n')|$, h is the Planck constant, c_0 is the speed of light in vacuum, $g(n) = 2n^2$ is the statistical weight, and $f_{n,n'}$ is the oscillator strength listed in Table II. The radiative excitation rate coefficient $A(n,n')$ for $n < n'$ is assumed to be zero.

The radiative exciton-formation rate coefficient $\beta(n)$ is

$$\beta(n) = \frac{2^8}{3\sqrt{3}}\sqrt{\pi}a_X^2\left(\frac{E_B(1)}{\mu c_0^2}\right)^2 c_0\left(\frac{E_B(n)}{k_BT_e}\right)^{3/2} \times \exp\left(\frac{E_B(n)}{k_BT_e}\right)\int_{E_B(n)/(k_BT_e)}^{\infty}\frac{e^{-x}}{x}dx, \tag{4}$$

where k_B is the Boltzmann constant.

For $N_e < 10^{18}$ cm^{-3} and $10 \leqslant T_e \leqslant 300$ K, the transition rates of $A(n,n')$ and $\beta(n)N_e$ are lower than 10^5 s^{-1}, and are also lower than 0.01% of the phononic transition rates shown in the next section. Thus, $A(n,n')$ and $\beta(n)$ affect little the results of the population densities.

TABLE I. Parameters used in our calculation for free A excitons in bulk GaN. m_0 is the electron rest mass. ϵ_0 is the dielectric constant of vacuum. h and $\hbar$ are the Planck constants. e_0 is the elementary charge. q is the phonon wave number.

Electron effective mass	m_e	$0.20m_0$	Ref. [46]
Hole effective mass	m_h	$1.76m_0$	Ref. [46]
Exciton effective reduced mass	μ	$0.180m_0$	$\mu^{-1} = m_e^{-1} + m_h^{-1}$
Static dielectric constant	ϵ_s	$9.5\epsilon_0$	Ref. [47]
High-frequency dielectric constant	ϵ_∞	$5.35\epsilon_0$	Ref. [47]
1S-exciton Bohr radius	a_X	27.99 Å	$a_X = 4\pi\epsilon_s\hbar^2/(\mu e_0^2)$
1S-exciton binding energy	$E_B(1)$	27.07 meV	$E_B(1) = \mu e_0^4/(8\epsilon_s^2h^2)$
Mass density	ρ	6.15 g/cm^3	Ref. [48]
Acoustic deformation potential (conduction band)	D_e	8.3 eV	Ref. [48]
Acoustic deformation potential (valence band)	D_h	−8.3 eV	Ref. [48]
Piezoelectric constant	$e_{\rm PZ}$	0.73 C/m^2	Ref. [49]
Lattice constant of the wurtzite a axis	a_L	3.189 Å	Ref. [50]
Lattice constant of the wurtzite c axis	c_L	5.185 Å	Ref. [50]
Effective isotropic lattice constant	$a_{\rm eff}$	2.881 Å	See text in Sec. III B
Longitudinal-optical (LO) phonon energy	$E_q^{\rm LO}$	$90.51 - 3.720\sin^4\frac{a_{\rm eff}q}{2}$ meV	Ref. [51] (Γ to M point)
Longitudinal-acoustic (LA) phonon energy	$E_q^{\rm LA}$	$37.82\sin\frac{a_{\rm eff}q}{2}$ meV	Ref. [51] (Γ to M point)

TABLE II. Oscillator strength $f_{n,n'}$. The last row shows $f_{n,c}$ for the continuum. The values excluding $f_{5,c}$ are from Table 3.1(b) of Ref. [44]. $f_{5,c}$ is obtained from $f_{n,c} = \frac{8}{3\sqrt{3}\pi}\frac{1}{n}\langle g_{bf}\rangle$ with the assumption of the Gaunt factor $\langle g_{bf}\rangle = 1$.

n'	$n = 1$	$n = 2$	$n = 3$	$n = 4$	$n = 5$
2	0.4162				
3	0.0791	0.641			
4	0.0290	0.120	0.841		
5	0.0139	0.045	0.150	1.038	
c	0.4350	0.231	0.160	0.124	0.0980

The electron-collisional excitation rate coefficient $C(n,n')$ for $n < n'$ is

$$C(n,n') = \int_{E(n,n')}^{\infty} \sigma_{n,n'}(E_e) f_M(E_e) v \, dE_e \tag{5a}$$

$$= 8a_X^2 \sqrt{\frac{2\pi}{\mu k_B T_e}} \frac{[E_B(1)]^2}{E(n,n')} f_{n,n'} \int_{E(n,n')/(k_B T_e)}^{\infty} \frac{e^{-x}}{x} dx, \tag{5b}$$

where $\sigma_{n,n'}(E_e)$ is the electron-collisional excitation cross section given by

$$\sigma_{n,n'}(E_e) = 4\pi a_X^2 \left(\frac{E_B(1)}{E(n,n')}\right)^2 f_{n,n'} \frac{E(n,n')}{E_e} \ln \frac{E_e}{E(n,n')}. \tag{6}$$

v is the electron velocity. $E_e = (1/2)\mu v^2$ is the electron kinetic energy. $f_M(E_e)$ is the Maxwellian velocity distribution function for E_e given by

$$f_M(E_e) = 2\sqrt{\frac{E_e}{\pi}} \frac{1}{(k_B T_e)^{3/2}} \exp\left(-\frac{E_e}{k_B T_e}\right). \tag{7}$$

The electron-collisional deexcitation rate coefficient $C(n,n')$ for $n > n'$ is

$$C(n,n') = \frac{g(n')}{g(n)} \exp\left(\frac{E(n',n)}{k_B T_e}\right) C(n',n), \tag{8}$$

where the detailed balance of the Boltzmann distribution between processes of $C(n,n')$ and $C(n',n)$ is assumed.

The electron-collisional exciton-dissociation rate coefficient $S(n)$ is

$$S(n) = \int_{E_B(n)}^{\infty} \sigma_{n,c}(E_e) f_M(E_e) v \, dE_e \tag{9a}$$

$$= 8a_X^2 \sqrt{\frac{2\pi}{\mu k_B T_e}} \frac{[E_B(1)]^{11/4}}{[E_B(n)]^{7/4}} f_{n,c} \times \int_{E_B(n)/(k_B T_e)}^{\infty} \frac{e^{-x}}{x} dx, \tag{9b}$$

where $\sigma_{n,c}(E_e)$ is the electron-collisional exciton-dissociation cross section given by

$$\sigma_{n,c}(E_e) = 4\pi a_X^2 \left(\frac{E_B(1)}{E_B(n)}\right)^{11/4} f_{n,c} \frac{E_B(n)}{E_e} \ln \frac{E_e}{E_B(n)}. \tag{10}$$

$f_{n,c}$ is the oscillator strength from the state of n to the continuum, which is listed in the last row of Table II.

The electron-collisional exciton-formation rate coefficient $\alpha(n)$ is

$$\alpha(n) = \frac{g(n)}{2} \left(\frac{2\pi\hbar^2}{\mu k_B T_e}\right)^{3/2} \exp\left(\frac{E_B(n)}{k_B T_e}\right) S(n), \tag{11}$$

where the detailed balance of the Saha-Boltzmann distribution between the processes of $S(n)$ and $\alpha(n)$ is assumed.

Figure 2 shows dependence of $C(1,n)$, $C(n,1)$, $S(n)$, and $\alpha(n)$ on T_e. The excitation and exciton-dissociation rate coefficients $C(1,n)$ and $S(n)$ increase as T_e increases. The deexcitation and exciton-formation rate coefficients $C(n,1)$ and $\alpha(n)$ increase and decrease, respectively, as T_e increases.

As shown in Figs. 2(a) and 2(b), the excitation or deexcitation rate coefficients $C(n,n')$ increase with the decrease in $E(n,n')$ (the energy difference between n and n'). The exciton-dissociation and formation rate coefficients $S(n)$ and $\alpha(n)$ also increase with the decrease in $E_B(n)$ (the energy difference between n and the continuum). For $n \geqslant 2$, $S(n)$ is higher than $C(1,n)$ because $E_B(n) < E(1,n)$. This relation indicates stronger coupling of the states of $n \geqslant 2$ with the continuum than with $n = 1$.

B. Phononic rate coefficients

The phononic rate coefficients $W_{XX}(n,n')$, $W_{XC}(n)$, and $W_{CX}(n)$ are calculated using Fermi's "golden rule." The wave number at the edge of the first Brillouin zone is set to be π/a_{eff}, where a_{eff} is the effective isotropic lattice constant. The value of a_{eff} is determined such that the volume of the first Brillouin zone of the isotropic system, $(4/3)\pi(\pi/a_{\text{eff}})^3$, is equal to that of wurtzite, $16\pi^3/(\sqrt{3}a_L^2 c_L)$. Here, a_L and c_L are the lattice constants of the a and c axes, respectively, which are shown in Table I.

The phononic excitation and deexcitation rate coefficient $W_{XX}(n,n')$ is

$$\begin{aligned} W_{XX}(n,n') = {} & \sum_{I=\text{FR,DP,PZ}} \sum_{\pm} \frac{2}{g(n)} \sum_{l,m,l',m'} \iint \left(n_q + \frac{1}{2} \pm \frac{1}{2}\right) \\ & \times \frac{2\pi}{\hbar} \left|D^I_{v,v'}(\vec{q})\right|^2 \delta(E_{K'} - E_B(n') \\ & - [E_K - E_B(n)] \pm E_q) \\ & \times f_M(M,\vec{K},T_X) d^3K \frac{V_{\text{int}}}{(2\pi)^3} d^3q, \end{aligned} \tag{12}$$

where I denotes the mechanism of the interaction between excitons (or free carriers) and phonons. These mechanisms are Fröhlich (FR) interaction with longitudinal-optical (LO) phonons, deformation potential (DP) interaction with longitudinal-acoustic (LA) phonons, and piezoelectric (PZ) interaction with LA phonons. The symbol of "±" denotes the phonon emission (+) and absorption (−). $\vec{q}$ and $\vec{K}$ are

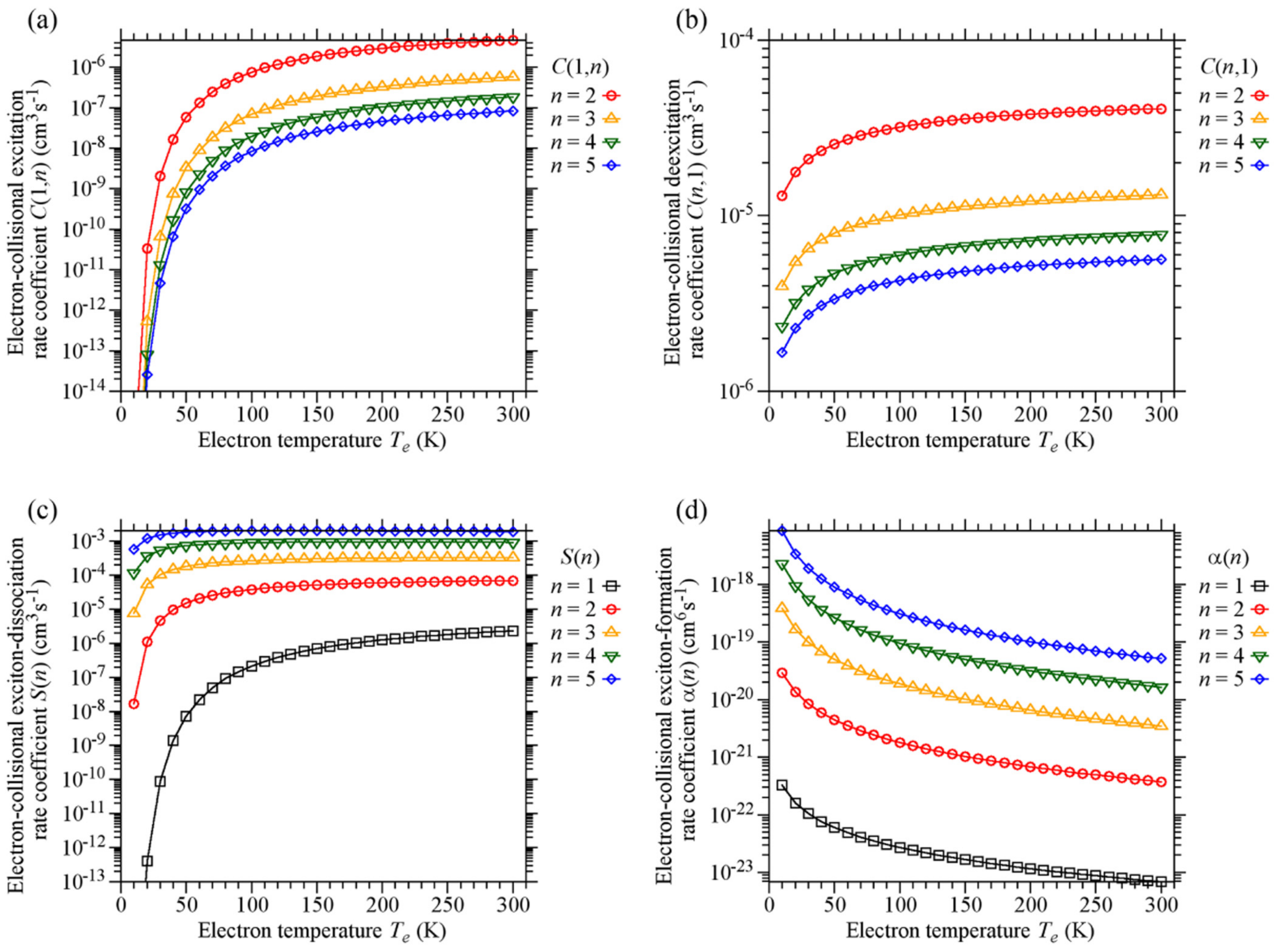

FIG. 2. Dependence of the electron-collisional rate coefficients (a) $C(1,n)$, (b) $C(n,1)$, (c) $S(n)$, and (d) $\alpha(n)$ on the electron temperature T_e.

wave vectors of phonons and excitons, respectively. $V_{\rm int}$ is the effective interaction volume. E_q is LO or LA phonon energy ($E_q = E_q^{\rm LO}$ for FR or $E_q = E_q^{\rm LA}$ for DP and PZ, which are shown in Table I). $n_q = 1/\{\exp[E_q/(k_BT_L)] - 1\}$ is the phonon occupation number (Bose-Einstein distribution). δ is the delta function. The exciton wave vector $\overrightarrow{K}'$ after the transition is determined by the momentum conservation

$$\overrightarrow{K} = \overrightarrow{K}' \pm \overrightarrow{q}. \tag{13}$$

$E_K = \hbar^2K^2/(2M)$ is the exciton kinetic energy. $f_M(m_p,\overrightarrow{k},T_p)$ is the Maxwellian velocity distribution function for particles with mass m_p, wave vector $\overrightarrow{k}$, and temperature T_p, which is given by

$$f_M(m_p,\overrightarrow{k},T_p) = \left(\frac{\hbar^2}{2\pi m_p k_B T_p}\right)^{3/2} \exp\left(-\frac{\hbar^2k^2}{2m_pk_BT_p}\right). \tag{14}$$

ν denotes the set of (n,l,m). The effective coupling constant $D^I_{\nu,\nu'}(\overrightarrow{q})$ is [52]

$$D^I_{\nu,\nu'}(\overrightarrow{q}) = C^I_{e,q}S_{\nu,\nu'}(\beta\overrightarrow{q}) - C^I_{h,q}S_{\nu,\nu'}(-\alpha\overrightarrow{q}), \tag{15}$$

where $\beta = m_h/M$ and $\alpha = m_e/M$. The coupling constant $C^I_{\sigma,q}$ ($\sigma = e,h$) is [52,53]

$$C^{\rm FR}_{\sigma,q} = e_0\left[\frac{E_q^{\rm LO}}{2V_q}\left(\frac{1}{\epsilon_\infty} - \frac{1}{\epsilon_s}\right)\right]^{1/2}\frac{1}{q}, \tag{16a}$$

$$C^{\rm DP}_{\sigma,q} = \frac{\hbar}{\left(2\rho E_q^{\rm LA}V_q\right)^{1/2}}D_\sigma q, \tag{16b}$$

$$C^{\rm PZ}_{\sigma,q} = \frac{e_0 e_{\rm PZ}\hbar}{\epsilon_s\left(2\rho E_q^{\rm LA}V_q\right)^{1/2}}, \tag{16c}$$

where V_q is the effective phonon volume. As in Ref. [52], $V_q = V_{\rm int}$ is assumed. Other parameters are listed in Table I. The exciton form factor $S_{\nu,\nu'}(\overrightarrow{k})$ is [52]

$$S_{\nu,\nu'}(\overrightarrow{k}) = \int d^3r\,\Phi^*_{\nu'}(\overrightarrow{r})e^{i\overrightarrow{k}\cdot\overrightarrow{r}}\Phi_\nu(\overrightarrow{r}), \tag{17}$$

where $\overrightarrow{r}$ is the real-space coordinate and $\Phi_\nu(\overrightarrow{r})$ is the hydrogenic wave function of excitons.

The phononic exciton-dissociation rate coefficient $W_{XC}(n)$ is

$$W_{XC}(n) = \sum_{I=\mathrm{FR,DP,PZ}} \sum_{\pm} \frac{2}{g(n)} \sum_{l,m} \iiint \left(n_q + \frac{1}{2} \pm \frac{1}{2}\right) \times \frac{2\pi}{\hbar} |\tilde{D}^I_{\pm}|^2 \delta(E_e + E_h - [E_K - E_B(n)] \pm E_q) \times \frac{V_{eh}}{(2\pi)^3} d^3k_h f_M(M,\vec{K},T_X) d^3K \frac{V_{\mathrm{int}}}{(2\pi)^3} d^3q, \quad (18)$$

where V_{eh} is the normalization volume for electrons and holes. $\vec{k}_e$ and $\vec{k}_h$ are the wave vectors of electrons and holes, respectively. $\vec{k}_e$ is determined by the momentum conservation

$$\vec{K} = \vec{k}_e + \vec{k}_h \pm \vec{q}. \quad (19)$$

$E_e = \hbar^2 k_e^2/(2m_e)$ and $E_h = \hbar^2 k_h^2/(2m_h)$ are the electron and hole kinetic energy, respectively. The effective coupling constant $\tilde{D}^I_{\pm}$ is [52]

$$\tilde{D}^I_{\pm} = C^I_{e,q} S_\nu(\vec{q}_e) - C^I_{h,q} S_\nu(\vec{q}_h), \quad (20a)$$

$$\vec{q}_e \equiv \beta(\vec{k}_e \pm \vec{q}) - \alpha \vec{k}_h, \quad (20b)$$

$$\vec{q}_h \equiv \beta \vec{k}_e - \alpha(\vec{k}_h \pm \vec{q}). \quad (20c)$$

The form factor $S_\nu(\vec{k})$ is [52,54]

$$S_\nu(\vec{k}) = \int d^3r \frac{1}{\sqrt{V^{\mathrm{PW}}_{eh}}} e^{i\vec{k}\cdot\vec{r}} \Phi_\nu(\vec{r}), \quad (21)$$

where V^{PW}_{eh} is the normalization volume for the plane waves of electrons and holes. $V^{\mathrm{PW}}_{eh} = V_{eh}$ is assumed.

The phononic exciton-formation rate coefficient $W_{CX}(n)$ is

$$W_{CX}(n) = \sum_{I=\mathrm{FR,DP,PZ}} \sum_{\pm} \sum_{l,m} \iiint \left(n_q + \frac{1}{2} \pm \frac{1}{2}\right) \times \frac{2\pi}{\hbar} |\tilde{D}^I_{\mp}|^2 \delta(E_K - E_B(n) - (E_e + E_h) \pm E_q) \times V^{\mathrm{int}}_{eh} f_M(m_e,\vec{k}_e,T_e) d^3k_e f_M(m_h,\vec{k}_h,T_e) d^3k_h \times \frac{V_{\mathrm{int}}}{(2\pi)^3} d^3q, \quad (22)$$

where V^{int}_{eh} is the interaction volume between electrons and holes. $V^{\mathrm{int}}_{eh} = V^{\mathrm{PW}}_{eh}$ is assumed. $\vec{K}$ is determined by the momentum conservation

$$\vec{k}_e + \vec{k}_h = \vec{K} \pm \vec{q}. \quad (23)$$

Figure 3 shows the dependence of $W_{XX}(1,2)$ on T_X at $T_L = 10$ K and on T_L at $T_X = 10$ K. As T_X increases at $T_L = 10$ K, $W_{XX}(1,2)$ of the LO phonon emission process ("FR, em") drastically increases compared to the other processes. For $T_X > 180$ K, $W_{XX}(1,2)$ of the LO phonon emission is dominant over the LA phonon emission ("DP, em" and "PZ, em"). As T_L increases at $T_X = 10$ K, $W_{XX}(1,2)$ of the LO phonon absorption increases and becomes higher than 10^{10} s^{-1}, while those of the other processes remain lower than 10^4 s^{-1}.

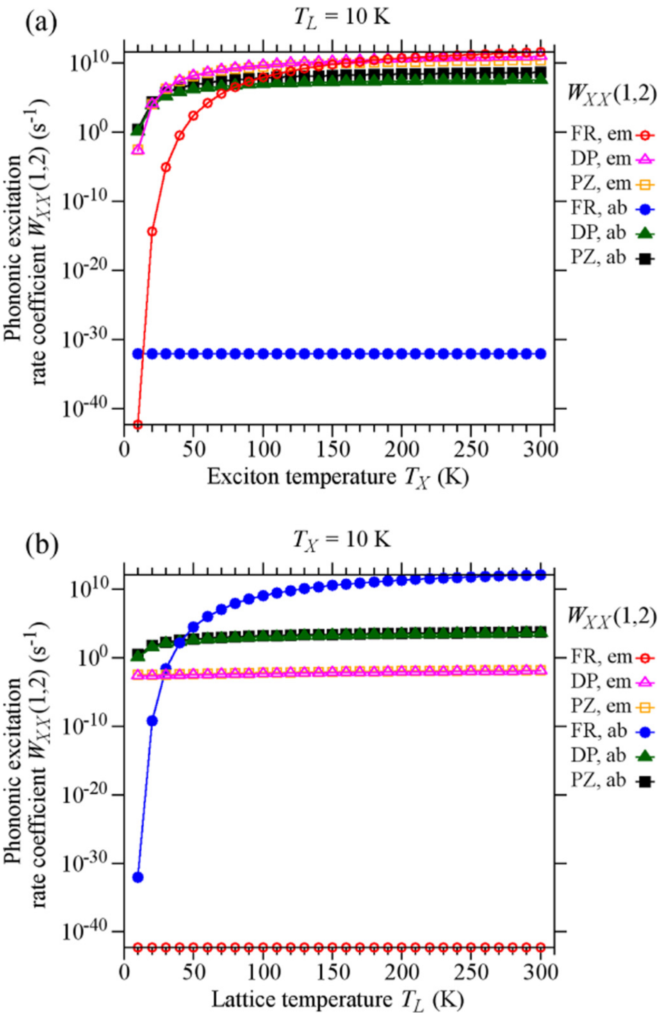

FIG. 3. Dependence of $W_{XX}(1,2)$ on (a) T_X and (b) T_L. "em" and "ab" denote the emission and absorption of phonons, respectively.

Figure 4 shows the dependence of $W_{XX}(1,n)$ and $W_{XX}(n,1)$ on $T_X = T_L$. As the temperatures increase or $E(1,n)$ decreases, $W_{XX}(1,n)$ and $W_{XX}(n,1)$ both increase. This tendency is similar to those of the electron-collisional rate coefficients shown in Figs. 2(a) and 2(b).

Figure 5 shows the dependence of the $1S$-exciton dissociation rate on E_K, which is denoted by $W_{XCK}(1)$ satisfying

$$W_{XC}(1) = \sum_{I=\mathrm{FR,DP,PZ}} \sum_{\pm} \int W_{XCK}(1) f_M(M,\vec{K},T_X) d^3K. \quad (24)$$

The $1S$-exciton dissociation with the LA phonon emission is forbidden for $E_K < E_B(1) = 27$ meV owing to the energy conservation. Because the minimum energy of the LO phonon is 87 meV, the dissociation with the LO phonon emission is forbidden for $E_K < 114$ meV (the sum of 27 and 87 meV). As E_K increases in the range of $E_K > 120$ meV, the dissociation rate of this process drastically increases compared to the other processes. As for the phonon absorption, LO and LA phonon absorption processes are dominant in the range of $E_K < 30$ meV and $E_K > 40$ meV, respectively. The scattering of some data points (sharp peaks) such as "DP, ab" at

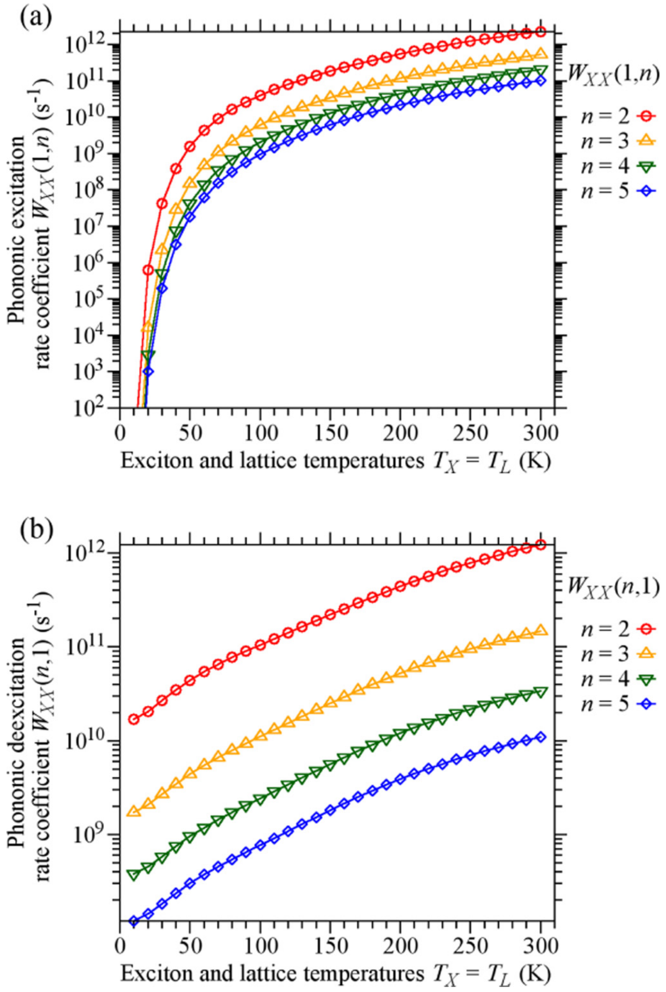

FIG. 4. Dependence of (a) $W_{XX}(1,n)$ and (b) $W_{XX}(n,1)$ on $T_X = T_L$.

$E_K = 118\,\text{meV}$ is attributed to the finite division number of numerical integration for $W_{XC}(n)$.

Figure 6 shows the dependence of the exciton-dissociation rate coefficient $W_{XC}(1)$ on T_L at $T_X = 10\,\text{K}$. This dependence is similar to that of $W(1,2)$ in Fig. 3(b). For $T_L \geqslant 40\,\text{K}$, $W_{XC}(1)$ of the LO phonon absorption is more than 10^4 times higher than that of the other processes. This is because $W_{XCK}(1)$ of the LO phonon absorption is dominant over the other processes for $E_K < 20\,\text{meV}$ ($k_B T_X = 0.86\,\text{meV}$ at $T_X = 10$ K), as shown in Fig. 5.

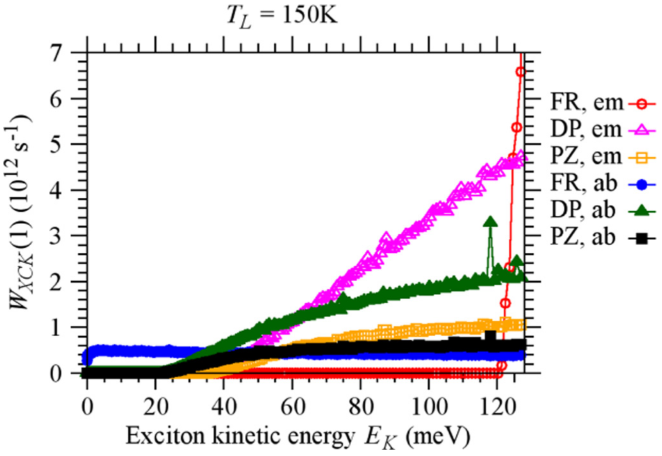

FIG. 5. Dependence of the phononic exciton-dissociation rate $W_{XCK}(1)$ on E_K.

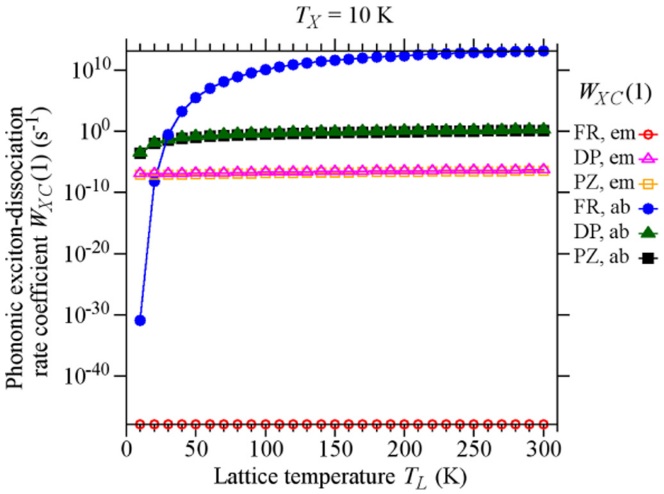

FIG. 6. Dependence of $W_{XC}(1)$ on T_L.

Figure 7 shows the dependence of $W_{XC}(n)$ on $T_X = T_L$ and $W_{CX}(n)$ on $T_e = T_L$. As T_X and T_L increase, $W_{XC}(n)$ increases. The increase in $W_{XC}(n)$ is higher for lower n, particularly below 50 K. As $E_B(n)$ decreases, $W_{XC}(n)$ and $W_{CX}(n)$ both increase. These tendencies are similar to those of the electron-collisional rate coefficients shown in Figs. 2(c) and 2(d).

In the case of $T_e = T_X = T_L = T$, it is possible to mathematically prove that the phononic rate coefficients of Eqs. (12), (18), and (22) satisfy

$$W_{XX}(n,n') = \frac{g(n')}{g(n)} \exp\left(\frac{E_B(n') - E_B(n)}{k_B T}\right) W_{XX}(n',n), \tag{25}$$

$$W_{CX}(n) = \frac{g(n)}{2} \left(\frac{2\pi\hbar^2}{\mu k_B T}\right)^{3/2} \exp\left(\frac{E_B(n)}{k_B T}\right) W_{XC}(n). \tag{26}$$

These equations correspond to the detailed balance conditions of the Saha-Boltzmann distribution.

C. Exciton-recombination rate coefficient

In this section, the applied value of the exciton-recombination rate coefficient (probability) $P_{\text{rec}}(n)$ in Eq. (1c) is presented. The nonradiative recombination processes are excluded for this applied value, though the effects of the nonradiative recombination are also discussed in our results of the population distribution and decay time in the following sections.

The radiative decay time (or lifetime) of $1S$ excitons in bulk GaN has been estimated experimentally in many studies [12,25,26,33,55–57]. However, the decay time differs from the recombination time defined as $\tau_{\text{rec}}(n) \equiv 1/P_{\text{rec}}(n)$. This is due to the net population flux Γ_{others} except for the recombination,

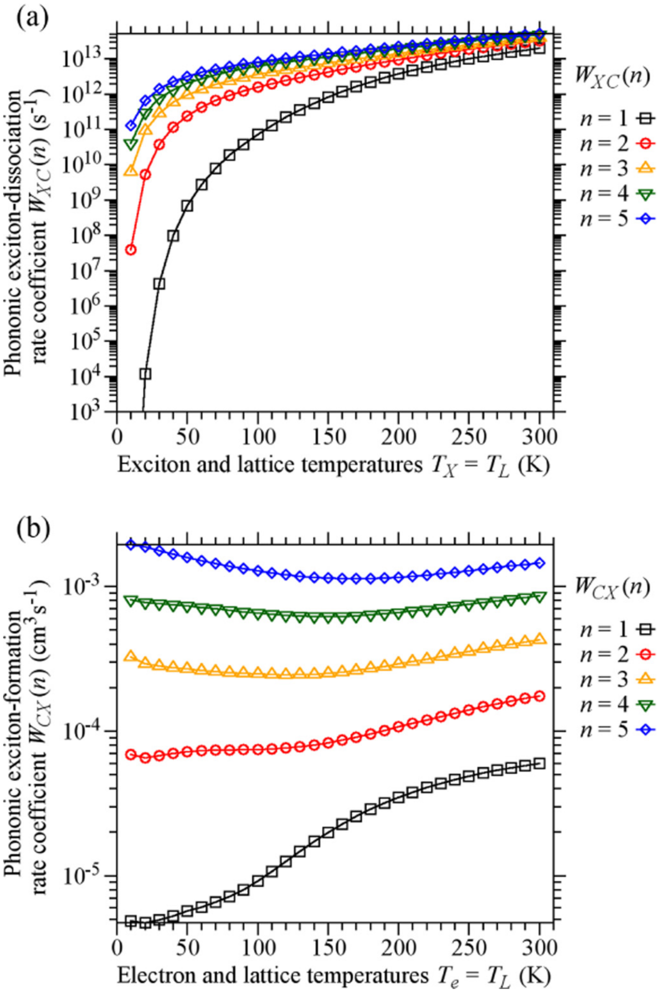

FIG. 7. Dependence of (a) $W_{XC}(n)$ on $T_X = T_L$ and (b) $W_{CX}(n)$ on $T_e = T_L$.

which is included in the rate equation expressed as

$$\frac{d}{dt}N_X(1) = -P_{\mathrm{rec}}(1)N_X(1) + \Gamma_{\mathrm{others}}. \tag{27}$$

In Ref. [25], the observed luminescence decay time of 2 to 17 ns (for 8 to 295 K) was interpreted as $\tau_{\mathrm{rec}}(1)$. However, this interpretation is questionable because the effect of Γ_{others} is neglected. In Ref. [26], $\tau_{\mathrm{rec}}(1)$ was experimentally estimated by taking into account the flux between the 1S-exciton and free-carrier levels, where the rate equations of N_e and $N_X(1)$ were analyzed and the Saha equation was assumed. This $\tau_{\mathrm{rec}}(1)$ in the range from 60 to 300 K agrees with the theoretical function in Ref. [24], which is

$$\tau_{\mathrm{rec}}(1) = (0.73\ \mathrm{ps/K}^{3/2})T_X^{3/2}. \tag{28}$$

At temperatures lower than tens of Kelvin, the radiative recombination probability is considered to be determined by the exciton-polariton picture, where the recombination probability depends on the sample thickness and quality [12,23,33,58]. This dependence on the sample thickness and quality possibly causes the variation in the decay time. According to Ref. [58], the theoretical value of $\tau_{\mathrm{rec}}(1)$ is 300 ps for the excited-region thickness $L = 0.1\,\mu$m, and is proportional to $L^{3/5}$. In our calculation, $\tau_{\mathrm{rec}}(1) = 300$ ps is adopted for $T_X \leqslant 55$ K. Equation (28) is applied for $T_X > 55$ K. That is, the recombination time for our calculation is

$$\tau_{\mathrm{rec}}(1) = \begin{cases} 300\ \mathrm{ps} & (T_X \leqslant 55\ \mathrm{K}) \\ (0.73\ \mathrm{ps/K}^{3/2})T_X^{3/2} & (T_X > 55\ \mathrm{K}) \end{cases}. \tag{29}$$

For $n \geqslant 2$, $\tau_{\mathrm{rec}}(n) = n^3\tau_{\mathrm{rec}}(1)$ is assumed.

IV. POPULATION DENSITY IN THE STEADY STATE

In this section, we show the dependence of the population densities in the steady state on the excitation rate and the temperatures. The rate equations (1) and (2) are solved for $N_X(n)$ and N_e by setting $\frac{d}{dt}N_X(n) = 0$ and $\frac{d}{dt}N_e = 0$. In this section, $R_{VX}(n)$ is assumed to be zero (i.e., the interband excitation).

Figure 8 shows the dependence of the population densities on the interband excitation rate R_{VC} at $T_e{=}T_X{=}T_L{=}10$ K. $N_X(1)$ and $N_X(2)$ are nearly proportional to R_{VC}. $N_X(3)$, $N_X(4)$, and $N_X(5)$ are also nearly proportional to R_{VC} in the range of $R_{VC} < 10^{14}$ cm^{-3} ns^{-1}, but deviate from the linear dependence with the increase in R_{VC}. The decrease in $N_e/N_X(1)$ by increasing R_{VC} is more distinct than that in $N_X(n)/N_X(1)$. This is because the increase in the exciton formation rate $[\alpha(n)N_e + W_{CX}(n)]N_e^2$ by increasing N_e is more drastic than the increase in the dissociation rate $[S(n)N_e + W_{XC}(n)]N_X(n)$ by increasing $N_X(n)$. In this paper, the maximum R_{VC} for the steady state is 7.5×10^{16} cm^{-3} ns^{-1}, which corresponds to laser excitation power of 33 mW for photon energy of 3.5 eV, penetration depth of 0.1 μm, and spot diameter of 0.1 mm. These values are reasonable for experimental situations.

Figures 9(a), 9(b), and 9(c) show the dependence of the population densities on T_e, T_X, and T_L, respectively. In these figures, the temperatures excluding the horizontal axis are fixed at 10 K. Figure 9(d) shows the dependence of the population densities on temperature T in the case of $T = T_e = T_X = T_L$.

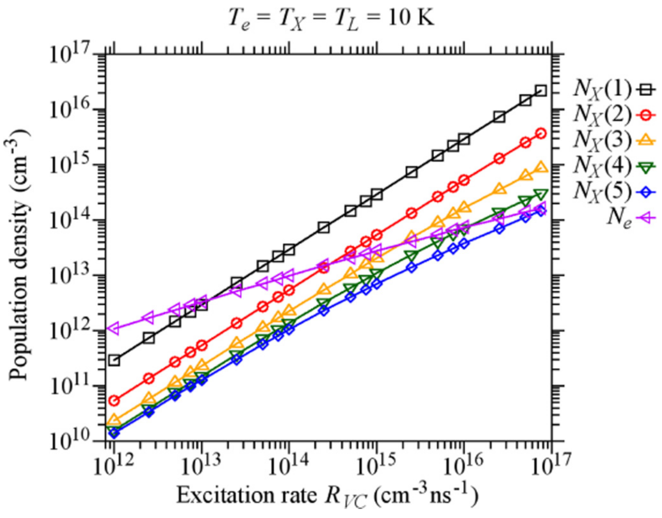

FIG. 8. Dependence of the population densities on the interband excitation rate R_{VC} in the steady state.

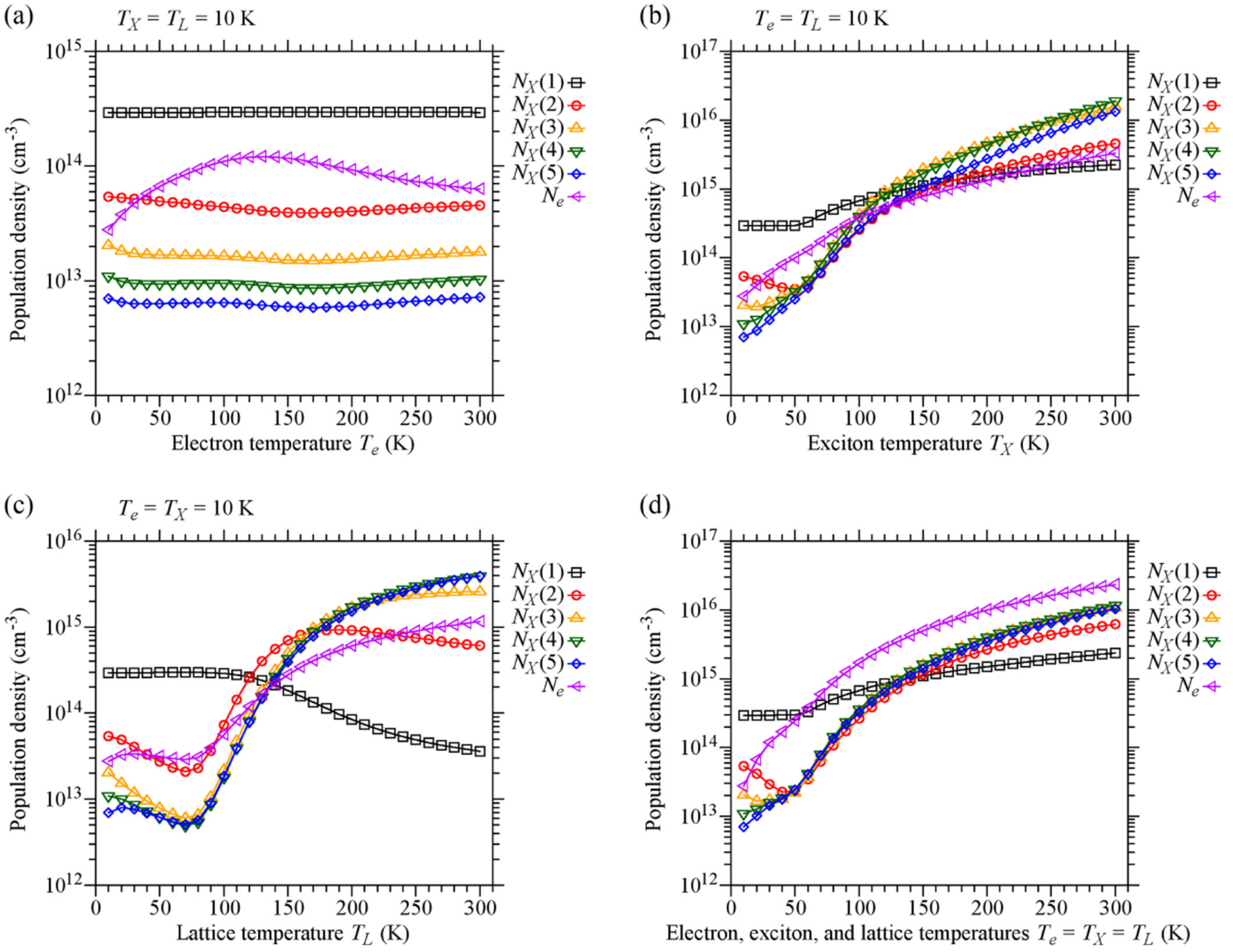

FIG. 9. Dependence of the population densities on (a) T_e, (b) T_X, (c) T_L, and (d) $T_e = T_X = T_L$ in the steady state. The temperatures excluding the horizontal axis are 10 K, and R_{VC} is 10^{15} cm^{-3} ns^{-1}.

In Fig. 9, R_{VC} is fixed at 10^{15} cm^{-3} ns^{-1}. Figures 9(b) and 9(d) show the increase in $N_X(1)$ with the increase in T_X and $T_e = T_X = T_L$, respectively. This is ascribed to the decrease in $P_{\rm rec}(1)$ with the increase in T_X. In many experimental studies, the nonradiative recombination rate is thought to increase with the increase in temperature. In this case, $N_X(1)$ possibly decreases as temperature increases.

As shown in Fig. 9(d), the ratios of the upper-level densities [$N_X(n)$ of $n \geqslant 2$ and N_e] to $N_X(1)$ increase as the temperature increases. The increase in the upper-level densities is due to the significant increase in the rate coefficients of excitation and dissociation from the 1S state with the increase in the temperatures, as compared to those of deexcitation and exciton formation (Figs. 2–7). The variation of $N_X(n)$ and N_e by increasing T_e in Fig. 9(a) is weak as compared to the increase of the upper-level densities by increasing T_X and T_L in Figs. 9(b) and 9(c), respectively. Thus, the increase of the upper-level densities in Fig. 9(d) is ascribed to the phononic processes rather than the electron-collisional processes.

The dominance of the phononic processes in the excitation and the dissociation from the 1S state is also seen in Fig. 10. In this figure, the width of the each arrow indicates the population transition flux (cm^{-3} ns^{-1}). For the excitation and the dissociation from the 1S state at 300 K, the phononic population fluxes are more than ten times higher than the electron-collisional fluxes. On the other hand, among the states of $n \geqslant 2$ and the continuum, the electron-collisional fluxes are comparable to the phononic fluxes. When the temperature increases, the fluxes between the states of $n \geqslant 2$ and the continuum become more dominant compared to those between the states of n and $n + 1$. This result indicates the increase in the coupling between the states of $n \geqslant 2$ and the continuum.

The increase of $N_e/N_X(1)$ by increasing temperature in Fig. 9 possibly partly explains the disappearance of the lasing based on the exciton-exciton scattering above 150 K in Ref. [4]. A further increase in N_e leads to the Mott transition. From Figs. 9(a) to 9(c), the increase in $N_e/N_X(1)$ is mainly ascribed to the increase in T_L. For further comparison with Ref. [4], it is necessary to treat higher density such as 10^{18} cm^{-3} and include the exciton-exciton scattering and the Mott transition.

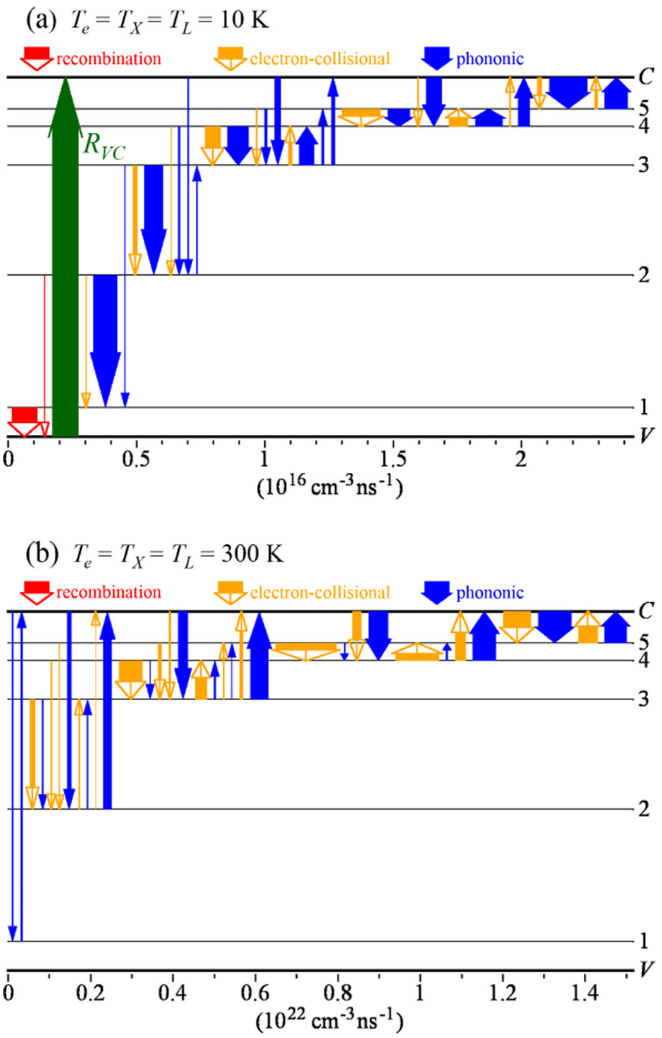

FIG. 10. Population transition fluxes in the energy-level diagram for $R_{VC} = 10^{15}$ cm^{-3} ns^{-1} and $T_e = T_X = T_L$ of (a) 10 K and (b) 300 K in the steady state [corresponding to Fig 9(d)]. The numbers, the letter V, and the letter C at the right edge denote n, the vacuum state (the valence band for electrons), and the continuum state (the conduction band for electrons), respectively. The width of each arrow indicates the magnitude of the flux, which corresponds to the scales at the bottoms of the graphs. For the fluxes lower than 0.1% of the sum of all fluxes, the arrows are omitted.

V. COMPARISON WITH THE SAHA-BOLTZMANN DISTRIBUTION

In this section, the population densities obtained by the rate equations are compared with the Saha-Boltzmann distribution when $T_e = T_X = T_L = T$ is assumed. In the Boltzmann distribution, $N_X(n)$ for $n \geqslant 2$ is given by [44]

$$N_{XB}(n) = N_X(1)\frac{g(n)}{g(1)}\exp\left(-\frac{E(1,n)}{k_BT}\right), \tag{30}$$

where $N_{XB}(n)$ denotes $N_X(n)$ obeying the Boltzmann distribution. In the Saha equation, N_e is given by [19,44]

$$(N_{eS})^2 = N_X(1)\left(\frac{\mu k_BT}{2\pi\hbar^2}\right)^{3/2}\exp\left(-\frac{E_B(1)}{k_BT}\right), \tag{31}$$

where N_{eS} denotes N_e obeying the Saha equation. In this paper, "the Saha-Boltzmann distribution" includes both the Boltzmann distribution and the Saha equation. We evaluate the difference from the Saha-Boltzmann distribution by using the parameters of $r_B(n) = N_X(n)/N_{XB}(n)$ and $r_S = N_e/N_{eS}$, where $N_X(n)$ and N_e are obtained by the rate equations in the steady state. $N_{XB}(n)$ and N_{eS} are calculated from Eqs. (30) and (31), respectively, using $N_X(1)$ obtained by the rate equations.

Figure 11 shows the dependence of $r_B(n)$ and r_S on the temperature T $(= T_e = T_X = T_L)$ for the total excited density $N_{\text{tot}} \equiv [\sum_{n\geqslant 1} N_X(n) + N_e]$ of 10^{13}, 10^{14}, 10^{15}, and 10^{16} cm^{-3}. The large open symbols and the small filled symbols correspond to the cases of the interband excitation [$R_{VC} \neq 0$ and $R_{VX}(n) = 0$] and the $1S$-resonant excitation [$R_{VX}(1) \neq 0$ and $R_{VC} = R_{VX}(n) = 0$ for $n \geqslant 2$], respectively. For the interband excitation below 20 K (insets), $r_B(n)$ and r_S are higher than 10^3 and 10, respectively, which means that the ratios of the upper-level densities [$N_X(n)$ for $n \geqslant 2$ and N_e] to $N_X(1)$ are much higher than those in the Saha-Boltzmann distribution. This significant increase in the upper-level densities is due to higher interband excitation flux R_{VC} than excitation flux from the $1S$ state as shown in Fig. 10(a). When the states of $n \geqslant 2$ are excluded, this phenomenon can be quantitatively understood as follows. Figure 12(a) shows the schematic diagram of the population fluxes in this case, where R_{VC}, $\Gamma_{\text{in}}(1)$, and $\Gamma_{\text{out}}(1)$ are balanced. The relation of $\Gamma_{\text{in}}(1) = \Gamma_{\text{out}}(1)$ gives $N_e^2 = N_X(1)P_{\text{rec}}(1)/[\alpha(1)N_e + W_{CX}(1)]$, which is more than two orders of magnitude higher than the value of Eq. (31). Thus, N_e is more than one order of magnitude higher than that of the Saha equation when the states of $n \geqslant 2$ are excluded. From the result in Fig. 11, such significant deviation from the Saha-Boltzmann distribution also occurs when the states of $n \geqslant 2$ are taken into account. Our calculation reveals that the Saha-Boltzmann distribution cannot be applied to the interband excitation at such low temperatures. In this case, it is unsuitable that the activation energy is estimated from exponential fitting of the luminescence intensity ratio between $n = 1$ and the upper levels.

On the other hand, for the $1S$-resonant excitation, deviation from the Saha-Boltzmann distribution below 20 K is minor as shown in Fig. 11. When the states of $n \geqslant 2$ are excluded for the $1S$-resonant excitation case as shown in Fig. 12(b), the flux Γ_{out}^e from the continuum to $n = 1$ is balanced with the flux Γ_{in}^e from $n = 1$ to the continuum. This relation of $\Gamma_{\text{out}}^e = \Gamma_{\text{in}}^e$ gives

$$[\alpha(1)N_e + W_{CX}(1)]N_e^2 = [S(1)N_e + W_{XC}(1)]N_X(1). \tag{32}$$

Substituting Eqs. (11) and (26) into Eq. (32) leads to the Saha equation [Eq. (31) for $N_{eS} = N_e$]. That is, the population densities exactly obey the Saha equation ($r_S = 1$) for any T and N_{tot}. When the states of $n \geqslant 2$ are taken into account, the population densities deviate from the Saha-Boltzmann distribution. Our results of r_S in Fig. 11 give quantitative correction for the two-level model (only $n = 1$ and the continuum). For $10 \leqslant T \leqslant 300$ K and $N_{\text{tot}} \leqslant 10^{16}$ cm^{-3}, $r_B(n)$ and r_S are in the range between 0.2 and 2.0. It is found that the deviation from the Saha-Boltzmann distribution becomes strong with the increase in N_{tot}.

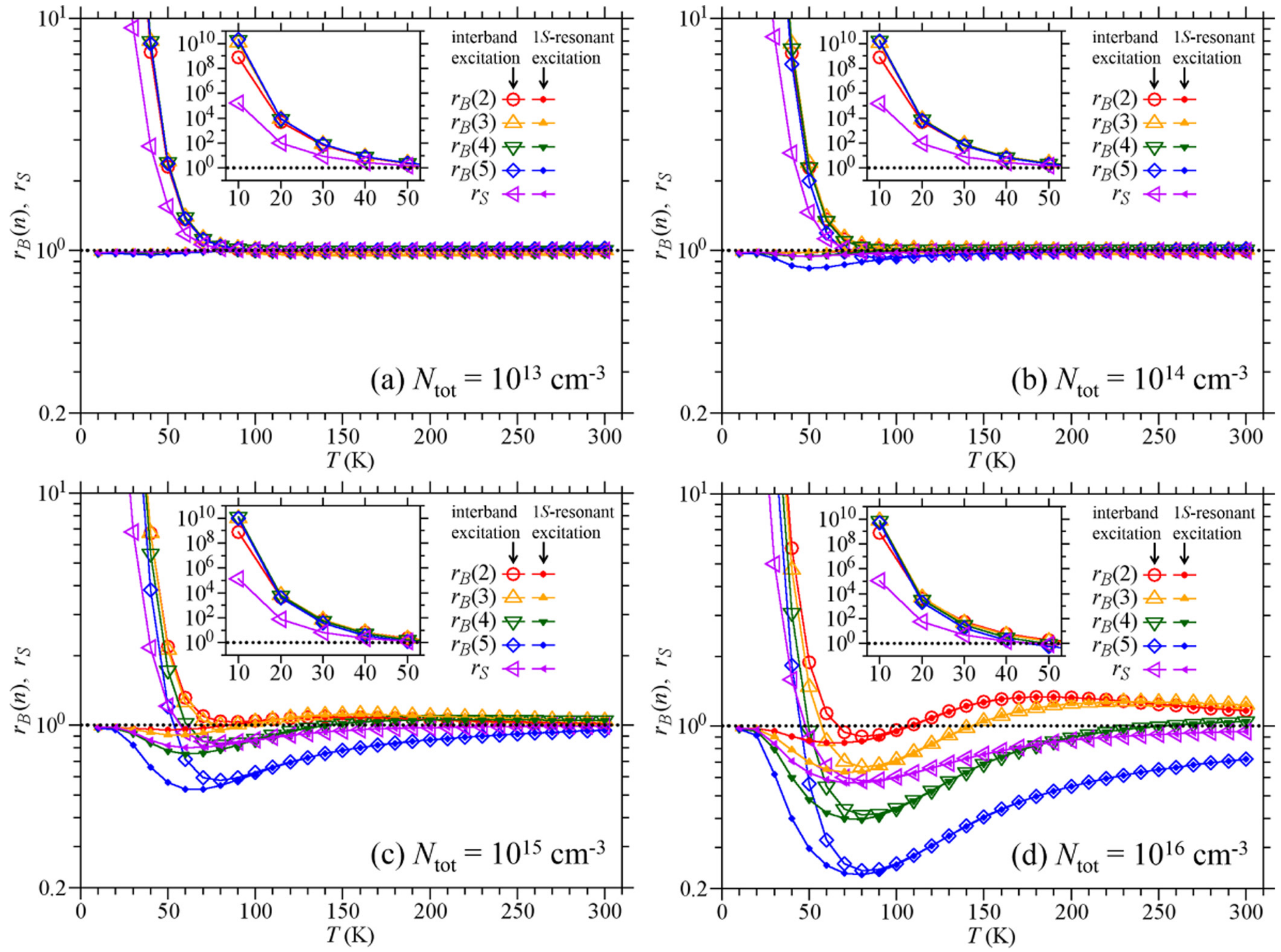

FIG. 11. Dependence of $r_B(n) = N_X(n)/N_{XB}(n)$ and $r_S = N_e/N_{eS}$ on the temperature T $(= T_e = T_X = T_L)$ for the interband excitation (large open symbols) and the $1S$-resonant excitation (small filled symbols). The insets show the interband excitation case below 50 K in the wide ranges of $r_B(n)$ and r_S. The dotted line denotes $r_B(n) = 1$ and $r_S = 1$.

Above 100 K, $r_B(n)$ and r_S for the $1S$-resonant excitation are approximately equal to those for the interband excitation. This is because the population fluxes among the exciton states of n and the continuum are much higher than $R_{VX}(1)$ or R_{VC} [as shown in Fig. 10(b)]. These high population fluxes are caused by the higher transition rates than 10^{10} s^{-1} such as $W_{XX}(n,n')$ and $W_{XC}(n)$ (Figs. 4 and 7). Once the value of $N_{\rm tot}$ is given as a constraint, the population balance for $N_X(n)$ and N_e is determined by these high population fluxes rather than by $R_{VX}(1)$ or R_{VC}. Thus, above 100 K, the population distribution is independent of the excitation path to the state of $n = 1$ or the continuum. Here, note that $R_{VX}(1)$ or R_{VC} is balanced with the recombination fluxes. The population distribution is also independent of the recombination rate $P_{\rm rec}(n)$ under the condition that $P_{\rm rec}(n)$ is lower than approximately 10% of the transition rates among the exciton states of n and the continuum. Therefore, even when the nonradiative recombination processes are taken into account, the values of r_S and $r_B(n)$ are the same as the above results under this condition.

Although the Saha-Boltzmann distribution has been often assumed in analyses of experimental data, our results show that the population densities significantly deviate from the Saha-Boltzmann distribution for the interband excitation below 20 K. Even for the $1S$-resonant excitation, or above 100 K, r_S deviates from unity owing to the states of $n \geqslant 2$. In Ref. [26], the Saha equation was utilized for the estimation of the radiative recombination probability above 60 K. In this temperature range, the significant deviation from the Saha equation does not occur, but r_S is in the range between 0.5 and 1.0 (for $N_{\rm tot} = 10^{16}$ cm^{-3}).

VI. DIFFERENCE BETWEEN DECAY TIME AND RECOMBINATION PROBABILITY

In this section, the time evolution and the decay time of $N_X(n)$ and N_e are shown for the case of $T_e = T_X = T_L = T$, which are calculated using the rate equations (1) and (2). Figure 13 shows the time evolution of $N_X(n)$ and N_e after a pulsed-interband excitation at $t = 0$. At $t = 0$, N_e is 10^{16} cm^{-3} and $N_X(n)$ is zero. For $t > 0$, R_{VC} and $R_{VX}(n)$ are zero. In this time evolution, the temperatures are assumed to be constant. The gray dashed line is the exponential curve fitted to $N_X(1)$ after the peak of $N_X(1)$. At 10 K in Fig. 13(a),

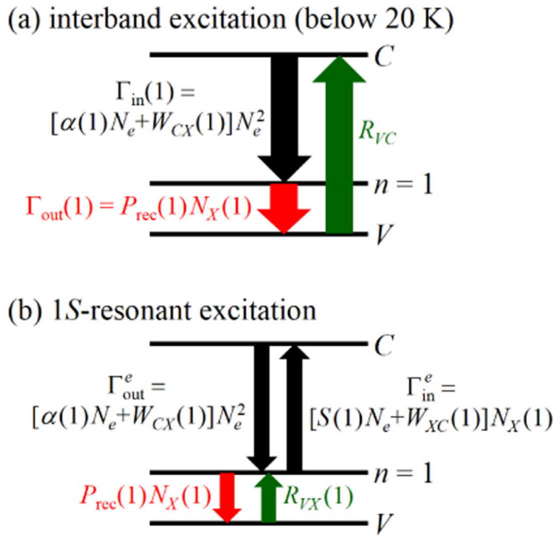

FIG. 12. Schematic diagram of the population fluxes when the states of $n \geqslant 2$ are excluded in the cases of (a) interband excitation below 20 K and (b) 1S-resonant excitation.

the 1S-exciton decay time $\tau_d(1) = 0.32$ ns is approximately equal to the recombination time $\tau_{rec}(1) \equiv 1/P_{rec}(1) = 0.30$ ns. However, at 300 K in Fig. 13(b), $\tau_d(1) = 143$ ns is more than ten times longer than $\tau_{rec}(1) = 3.8$ ns. This result disproves the conventional idea of $\tau_d(1) \approx \tau_{rec}(1)$ in experimental analyses such as Refs. [25,57]. The longer $\tau_d(1)$ than $\tau_{rec}(1)$ is due to the net population flux Γ_{others} from the upper levels ($n \geqslant 2$ and the continuum) to the 1S level, as indicated in Eq. (27). The increase in the ratios of the upper-level densities to $N_X(1)$ from 10 to 300 K (as in Secs. IV and V) leads to the increase in $\tau_d(1)/\tau_{rec}(1)$.

Figure 14 shows the dependence of $\tau_d(1)$ and $\tau_{rec}(1)$ on T for the interband excitation at the excitation density $N_{tot}|_{t=0} = 10^{16}$ cm^{-3}, where $N_{tot}|_{t=0}$ is the value of N_{tot} ($= N_e$) at $t = 0$. The value of $\tau_d(1)$ is obtained by the fitting in a time region of the decay of $N_X(1)$ from $N_X(1)|_{max}$ to $\exp(-2)N_X(1)|_{max}$, where $N_X(1)|_{max}$ is the maximum (peak) value of $N_X(1)$. $\tau_d(1)$ in our calculation disagrees with the law of $T^{3/2}$, though this law was applied to the temperature dependence of the luminescence decay time observed in Ref. [25]. Nonradiative recombination processes possibly affect the decay time in this reference.

Figure 15 shows the dependence of $\tau_d(1)/\tau_{rec}(1)$ on T for various excitation densities $N_{tot}|_{t=0}$. As T increases or $N_{tot}|_{t=0}$ decreases, $\tau_d(1)/\tau_{rec}(1)$ increases. This is attributed to the increase in the ratios of the upper-level densities to $N_X(1)$ with the increase in T or the decrease in N_{tot}. This increase in the fraction of the upper-level densities is indicated in Sec. IV and the Saha-Boltzmann distribution. As stated in Sec. V, the population distribution is independent of the recombination rate $P_{rec}(n)$ under the condition that $P_{rec}(n)$ is lower than approximately 10% of the transition rates among the exciton states of n and the continuum. Under this condition, the values of $\tau_d(1)/\tau_{rec}(1)$ in Fig. 15 are also independent of $P_{rec}(n)$. For example, let us assume that the nonradiative recombination rate of the 1S exciton is 10^{12} s^{-1} $= 1/(1\text{ps})$ at 300 K, which is lower than 10% of $W_{XC}(1) \approx 2\times10^{13}$ s^{-1}.

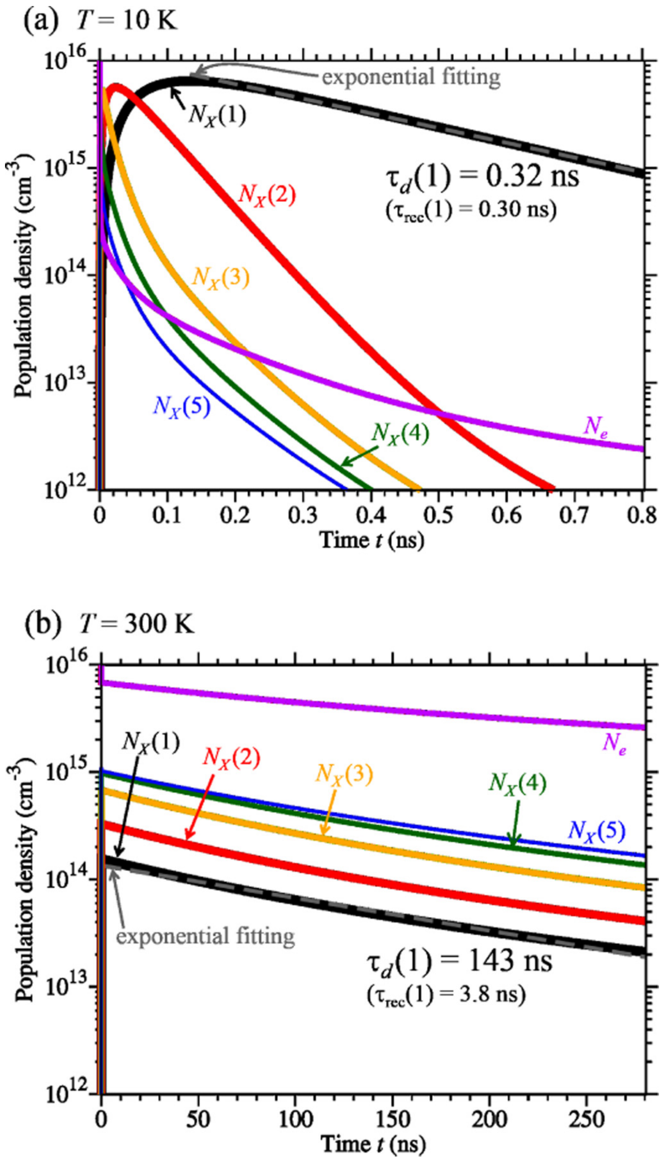

FIG. 13. Time evolution of $N_X(n)$ and N_e after a pulsed-interband excitation for (a) 10 K and (b) 300 K. At $t = 0$, N_e is 10^{16} cm^{-3} and $N_X(n)$ is zero. The gray dashed line is the exponential curve fitted to $N_X(1)$. $\tau_d(1)$ is the fitting decay time of $N_X(1)$. The 1S-exciton recombination time $\tau_{rec}(1) \equiv 1/P_{rec}(1)$ is also shown.

For $N_{tot}|_{t=0} = 10^{16}$ cm^{-3}, $\tau_d(1)$ is approximately 40 ps because of $\tau_d(1)/\tau_{rec}(1) \approx 4\times10^1$ in Fig. 15.

For $N_{tot}|_{t=0} = 10^{13}$ cm^{-3} in Fig. 15, $\tau_d(1)/\tau_{rec}(1)$ is approximately 2 even at 10 K. In the case of the pulsed 1S-resonant excitation for 10 K and $N_{tot}|_{t=0} \geqslant 10^{13}$ cm^{-3} [$N_{tot} = N_X(1)$ at $t = 0$], the upper-level densities are less than 0.01% of $N_X(1)$, as indicated in Sec. V. In this case, $\tau_d(1)$ is approximately equal to $\tau_{rec}(1)$. Above 100 K, the population distribution after the pulsed 1S-resonant excitation becomes approximately the same as that of the interband excitation within tens of picoseconds, which is ascribed to the transition rates higher than 10^{10} s^{-1}. After that, $N_X(1)$ decays with the time constant approximately equal to $\tau_d(1)$ in Fig. 15. Thus, above 100 K, the decay time differs from $\tau_{rec}(1)$ for both the 1S-resonant and interband excitation.

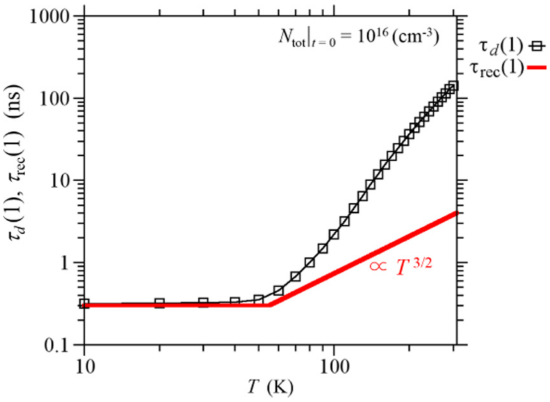

FIG. 14. Dependence of $\tau_d(1)$ (the decay time) and $\tau_{\mathrm{rec}}(1)$ (the inverse of the recombination probability) on the temperature T for the pulsed-interband excitation.

$\tau_d(1)/\tau_{\mathrm{rec}}(1)$ is approximately unity below 20 K and for $N_{\mathrm{tot}}|_{t=0} \geqslant 10^{14}\ \mathrm{cm}^{-3}$ in Fig. 15, though the ratios of the upper-level densities [at time of peak of $N_X(1)$] to $N_X(1)$ are more than ten times higher than those of the Saha-Boltzmann distribution as indicated in Sec. V. Even in this case, the upper-level densities are lower than $N_X(1)$ as indicated in Fig. 8, which is consistent with $\tau_d(1)/\tau_{\mathrm{rec}}(1) \approx 1$. Thus, the difference between $\tau_d(1)$ and $\tau_{\mathrm{rec}}(1)$ is not caused by the deviation from the Saha-Boltzmann distribution of the thermal equilibrium. Although the population densities above 100 K agree with the Saha-Boltzmann distribution within one order of magnitude (Fig. 11), $\tau_d(1)$ is more than ten times longer than $\tau_{\mathrm{rec}}(1)$ for some cases in Fig. 15.

For temperatures lower than tens of Kelvin, the observed luminescence decay time is scattered from tens of picoseconds to 2 ns [12,25,26,33,55–57]. Our results in Fig. 15 indicate that the population flux from the upper level to the 1S level does not cause this variation in the observed decay time for the low temperatures and for $\tau_{\mathrm{rec}}(1) \geqslant 300$ ps. This variation in the decay time is possibly ascribed to the dependence of the recombination probability on the sample thickness and quality in the exciton-polariton picture, as pointed out in Sec. III C.

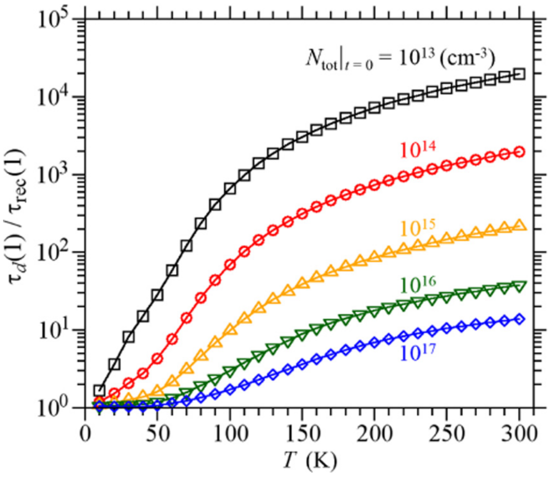

FIG. 15. Dependence of $\tau_d(1)/\tau_{\mathrm{rec}}(1)$ (decay time over recombination time of 1S excitons) on the temperature T for the pulsed-interband excitation. Each symbol corresponds to each value of the excitation density N_{tot} ($=N_e$) at $t = 0$.

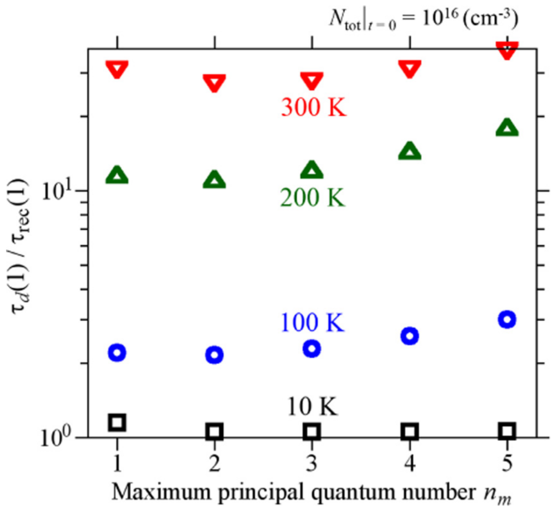

FIG. 16. Dependence of $\tau_d(1)/\tau_{\mathrm{rec}}(1)$ (decay time over recombination time of 1S excitons) on the maximum principal quantum number n_m for the pulsed-interband excitation. Each symbol corresponds to each temperature T.

Figure 16 shows dependence of $\tau_d(1)/\tau_{\mathrm{rec}}(1)$ on maximum principal quantum number n_m for the pulsed-interband excitation, where the states of $n > n_m$ are excluded. $\tau_d(1)/\tau_{\mathrm{rec}}(1)$ for n_m of 4 or 5 is up to approximately two times higher than that for $n_m \leqslant 3$. These results quantitatively reveal correction for the two-level model ($n_m = 1$) used in studies such as Ref. [26].

VII. LIMITATIONS OF CONVENTIONAL ANALYSES

Our model gives insights into the limitations of several conventional analyses. The ABC model is inappropriate below the Mott density because the phononic exciton-formation rate coefficient $W_{CX}(n)$ is much higher than the recombination rate coefficient B of free electrons and holes as pointed out in Sec. II. Also, the phononic exciton-dissociation rate coefficient $W_{XC}(n)$ is higher than $10^{11}\ \mathrm{s}^{-1}$ above 110 K (Fig. 7), which means that the ABC model is unsuitable if the time scale of the recombination of free electrons and holes is longer than hundreds of picoseconds.

Radiative and nonradiative recombination processes of excitons have sometimes been analyzed by Arrhenius plot and the formula of $1/[1 + \sum_j C_j \exp(-E_j/k_B T)]$, where j denotes the exciton-annihilation channel, C_j is constant, and E_j is the activation energy. This formula for the exciton system is derived from the rate equation expressed as

$$\frac{dN_X(1)}{dt} = G - \sum_j R_j N_X(1) - P_{\mathrm{rec}}(1) N_X(1) = 0, \quad (33)$$

$$R_j \propto \exp(-E_j/k_B T), \quad (34)$$

where G is the exciton-generation rate (constant) and R_j is the annihilation rate. However, it is assumed that the activation of a process characterized by E_j leads to the annihilation of excitons, and the regeneration (formation) of excitons is excluded. It is impossible to apply the above formula to the exciton-carrier system, where the dissociation and formation of excitons are balanced and the exciton-formation rate $W_{CX}(n)N_e^2$ strongly depends on temperature as indicated in Fig. 9(d).

Our model compensates for the weakness of the two-level model ($n = 1$ and the continuum). The correction for the Saha equation is given by r_S in Fig. 11. Particularly for the interband excitation below 20 K, the models assuming the Saha equation are obviously inappropriate. The decay time of the 1S-exciton population is enhanced (up to approximately two times) when the states of $n = 4$ and 5 are taken into account, as shown in Fig. 16. Figure 15 indicates the temperature and density ranges where the decay time is considerably longer than the inverse of the recombination probability. This result gives the limitation of the conventional model excluding the effect of the upper levels such as the continuum state.

VIII. SUMMARY AND CONCLUSIONS

The rate coefficients for transitions among free carriers and excitons of $n \leqslant 5$ have been theoretically calculated for bulk GaN. The dependence of the rate coefficients on the respective temperatures of electrons, excitons, and phonons (lattice) has been shown. The ratios of the upper-level densities to the 1S-exciton density increase as the excitation density decreases or the temperatures increase. The 1S-exciton dissociation is mainly caused by the phononic processes and the increase in the lattice temperature.

We have shown the values of $r_B(n)$ and r_S, which are the ratios of the population densities obtained by the rate equations to those of the Saha-Boltzmann distribution. For the interband excitation below 20 K, the population densities significantly deviate from the Saha-Boltzmann distribution [$r_B(n) > 10^3$ and $r_S > 10$] owing to the higher interband excitation flux than the excitation flux from the 1S state. For the 1S-resonant excitation or above 60 K, $r_B(n)$ and r_S are in the range between 0.2 and 2.0. The occupation of the states of $n \geqslant 2$ causes the deviation from the Saha equation. These results give the correction for the two-level model (only $n = 1$ and the continuum).

Our calculations have quantitatively revealed the difference between the 1S-population decay time $\tau_d(1)$ and the recombination probability $P_{\text{rec}}(1) = 1/\tau_{\text{rec}}(1)$. As the temperature increases or the excitation density decreases, $\tau_d(1)/\tau_{\text{rec}}(1)$ increases. At 300 K, $\tau_d(1)$ is more than ten times longer than $\tau_{\text{rec}}(1)$. These results disprove the conventional idea of $\tau_d(1) \approx \tau_{\text{rec}}(1)$, and show the temperature and density ranges where this idea is unsuitable. The limitation of the analyses neglecting the upper levels has been clarified.

We have constructed the basic model (PXR model) describing the densities of free carriers and excitons with several n in bulk system. The results of the population distribution in this model are also valid for the systems including the nonradiative recombination processes if the recombination rate is lower than approximately 10% of the transition rates among the states of excitons and free carriers. Our model gives insights into the limitations of the conventional analyses such as the ABC model, the Arrhenius plot, the two-level model, and the neglect of the upper levels. It is possible to use our model for other materials such as GaAs, AlN, and ZnO by changing the parameters in Table I and the recombination probability. More rigorous models for experiments can be developed by including other levels and transition processes such as exciton-exciton scattering, biexcitons, B and C excitons, impurity, and defects.

ACKNOWLEDGMENT

This work was partially supported by Japan Society for the Promotion of Science KAKENHI Grants No. JP16H06425 and No. JP17H02772.

---

[1] S. Chichibu, T. Azuhata, T. Sota, and S. Nakamura, J. Appl. Phys. **79**, 2784 (1996).

[2] H. Murotani, T. Kuronaka, Y. Yamada, T. Taguchi, N. Okada, and H. Amano, J. Appl. Phys. **105**, 083533 (2009).

[3] D. M. Bagnall, Y. F. Chen, Z. Zhu, T. Yao, M. Y. Shen, and T. Goto, Appl. Phys. Lett. **73**, 1038 (1998).

[4] S. Bidnyk, T. J. Schmidt, B. D. Little, and J. J. Song, Appl. Phys. Lett. **74**, 1 (1999).

[5] K. T. Tsen, R. P. Joshi, D. K. Ferry, A. Botchkarev, B. Sverdlov, A. Salvador, and H. Morkoç, Appl. Phys. Lett. **68**, 2990 (1996).

[6] D. Hägele, R. Zimmermann, M. Oestreich, M. R. Hofmann, W. W. Rühle, B. K. Meyer, H. Amano, and I. Akasaki, Phys. Rev. B **59**, R7797 (1999).

[7] A. Matulionis, J. Liberis, I. Matulionienė, M. Ramonas, L. F. Eastman, J. R. Shealy, V. Tilak, and A. Vertiatchikh, Phys. Rev. B **68**, 035338 (2003).

[8] L. Cavigli, R. Gabrieli, M. Gurioli, F. Bogani, E. Feltin, J.-F. Carlin, R. Butté, N. Grandjean, and A. Vinattieri, Phys. Rev. B **82**, 115208 (2010).

[9] K. Kyhm, L. Rota, and R. A. Taylor, Phys. Status Solidi A **208**, 1159 (2011).

[10] A. Vinattieri, F. Bogani, L. Cavigli, D. Manzi, M. Gurioli, E. Feltin, J.-F. Carlin, D. Martin, R. Butté, and N. Grandjean, Phys. Rev. B **87**, 075202 (2013).

[11] B. Monemar, P. P. Paskov, J. P. Bergman, A. A. Toropov, and T. V. Shubina, Phys. Status Solidi B **244**, 1759 (2007).

[12] B. Monemar, P. P. Paskov, J. P. Bergman, A. A. Toropov, T. V. Shubina, T. Malinauskas, and A. Usui, Phys. Status Solidi B **245**, 1723 (2008).

[13] M. C. Tam, A. M. C. Ng, A. B. Djurišić, and K. S. Wong, J. Appl. Phys. **112**, 023515 (2012).

[14] S. Chen, M. Yoshita, A. Ishikawa, T. Mochizuki, S. Maruyama, H. Akiyama, Y. Hayamizu, L. N. Pfeiffer, and K. W. West, Sci. Rep. **3**, 1941 (2013).

[15] C. Hauswald, T. Flissikowski, T. Gotschke, R. Calarco, L. Geelhaar, H. T. Grahn, and O. Brandt, Phys. Rev. B **88**, 075312 (2013).

[16] C. Hauswald, P. Corfdir, J. K. Zettler, V. M. Kaganer, K. K. Sabelfeld, S. Fernández-Garrido, T. Flissikowski, V. Consonni, T. Gotschke, H. T. Grahn, L. Geelhaar, and O. Brandt, Phys. Rev. B **90**, 165304 (2014).

[17] M. Palummo, M. Bernardi, and J. C. Grossman, Nano Lett. **15**, 2794 (2015).

[18] Y. Yamada, Y. Yamaji, and M. Imada, Phys. Rev. Lett. **115**, 197701 (2015).
[19] M. Beck, J. Hübner, M. Oestreich, S. Bieker, T. Henn, T. Kiessling, W. Ossau, and L. W. Molenkamp, Phys. Rev. B **93**, 081204(R) (2016).
[20] E. S. Khramtsov, P. A. Belov, P. S. Grigoryev, I. V. Ignatiev, S. Yu. Verbin, Yu. P. Efimov, S. A. Eliseev, V. A. Lovtcius, V. V. Petrov, and S. L. Yakovlev, J. Appl. Phys. **119**, 184301 (2016).
[21] C. Robert, D. Lagarde, F. Cadiz, G. Wang, B. Lassagne, T. Amand, A. Balocchi, P. Renucci, S. Tongay, B. Urbaszek, and X. Marie, Phys. Rev. B **93**, 205423 (2016).
[22] H. Wang, C. Zhang, W. Chan, C. Manolatou, S. Tiwari, and F. Rana, Phys. Rev. B **93**, 045407 (2016).
[23] L. C. Andreani, in *Confined Electrons and Photons*, edited by E. Burstein and C. Weisbuch, NATO ASI Series B: Physics Vol. 340 (Plenum, New York, 1995), pp. 57–112.
[24] A. Dmitriev and A. Oruzheinikov, J. Appl. Phys. **86**, 3241 (1999).
[25] Y. Zhong, K. S. Wong, W. Zhang, and D. C. Look, Appl. Phys. Lett. **89**, 022108 (2006).
[26] J. S. Im, A. Moritz, F. Steuber, V. Härle, F. Scholz, and A. Hangleiter, Appl. Phys. Lett. **70**, 631 (1997).
[27] Y. C. Shen, G. O. Mueller, S. Watanabe, N. F. Gardner, A. Munkholm, and M. R. Krames, Appl. Phys. Lett. **91**, 141101 (2007).
[28] Q. Dai, M. F. Schubert, M. H. Kim, J. K. Kim, E. F. Schubert, D. D. Koleske, M. H. Crawford, S. R. Lee, A. J. Fischer, G. Thaler, and M. A. Banas, Appl. Phys. Lett. **94**, 111109 (2009).
[29] P. Kivisaari, L. Riuttanen, J. Oksanen, S. Suihkonen, M. Ali, H. Lipsanen, and J. Tulkki, Appl. Phys. Lett. **101**, 021113 (2012).
[30] J. Piprek, F. Römer, and B. Witzigmann, Appl. Phys. Lett. **106**, 101101 (2015).
[31] Y. Iwata, R. G. Banal, S. Ichikawa, M. Funato, and Y. Kawakami, J. Appl. Phys. **117**, 075701 (2015).
[32] P. L. Gourley and J. P. Wolfe, Phys. Rev. B **25**, 6338 (1982).
[33] O. Brandt, J. Ringling, K. H. Ploog, H.-J. Wünsche, and F. Henneberger, Phys. Rev. B **58**, R15977 (1998).
[34] A. Chernikov, M. Koch, B. Laumer, T. A. Wassner, M. Eickhoff, S. W. Koch, and S. Chatterjee, Appl. Phys. Lett. **99**, 231910 (2011).
[35] M. A. Reshchikov, A. A. Kvasov, M. F. Bishop, T. McMullen, A. Usikov, V. Soukhoveev, and V. A. Dmitriev, Phys. Rev. B **84**, 075212 (2011).
[36] M. Kozák, F. Trojánek, and P. Malý, Phys. Status Solidi A **211**, 2244 (2014).
[37] M. A. Reshchikov, J. Appl. Phys. **115**, 103503 (2014).
[38] J. Barjon, P. Valvin, C. Brimont, P. Lefebvre, O. Brinza, A. Tallaire, J. Achard, F. Jomard, and M. A. Pinault-Thaury, Phys. Rev. B **93**, 115202 (2016).
[39] Y. Ishitani, K. Takeuchi, N. Oizumi, H. Sakamoto, B. Ma, K. Morita, H. Miyake, and K. Hiramatsu, J. Phys. D **49**, 245102 (2016).
[40] A. Tsukazaki, A. Ohtomo, M. Kawasaki, T. Makino, C. H. Chia, Y. Segawa, and H. Koinuma, Appl. Phys. Lett. **84**, 3858 (2004).
[41] M. V. Yakushev, R. W. Martin, A. V. Mudryi, and A. V. Ivaniukovich, Appl. Phys. Lett. **92**, 111908 (2008).
[42] M. M. Glazov, E. L. Ivchenko, G. Wang, T. Amand, X. Marie, B. Urbaszek, and B. L. Liu, Phys. Status Solidi B **252**, 2349 (2015).
[43] T. Fujimoto, J. Phys. Soc. Jpn. **47**, 265 (1979).
[44] T. Fujimoto, *Plasma Spectroscopy* (Clarendon, Oxford, 2004), Chaps. 1–4.
[45] S. Bieker, T. Henn, T. Kiessling, W. Ossau, and L. W. Molenkamp, Phys. Rev. Lett. **114**, 227402 (2015).
[46] M. Suzuki, T. Uenoyama, and A. Yanase, Phys. Rev. B **52**, 8132 (1995).
[47] J. A. S. Barker and M. Ilegems, Phys. Rev. B **7**, 743 (1973).
[48] B. E. Foutz, S. K. O'Leary, M. S. Shur, and L. F. Eastman, J. Appl. Phys. **85**, 7727 (1999).
[49] F. Bernardini, V. Fiorentini, and D. Vanderbilt, Phys. Rev. B **56**, R10024 (1997).
[50] D. C. Reynolds, D. C. Look, and B. Jogai, Solid State Commun. **99**, 873 (1996).
[51] T. Ruf, J. Serrano, M. Cardona, P. Pavone, M. Pabst, M. Krisch, M. D'Astuto, T. Suski, I. Grzegory, and M. Leszczynski, Phys. Rev. Lett. **86**, 906 (2001).
[52] P. E. Selbmann, M. Gulia, F. Rossi, E. Molinari, and P. Lugli, Phys. Rev. B **54**, 4660 (1996).
[53] S. Rudin, T. L. Reinecke, and B. Segall, Phys. Rev. B **42**, 11218 (1990).
[54] J. Singh, *Excitation Energy Transfer Processes in Condensed Matter* (Plenum, New York, 1994), Chaps. 1, 2, and 5.
[55] C. I. Harris, B. Monemar, H. Amano, and I. Akasaki, Appl. Phys. Lett. **67**, 840 (1995).
[56] G. D. Chen, M. Smith, J. Y. Lin, H. X. Jiang, S.-H. Wei, M. Asif Khan, and C. J. Sun, Appl. Phys. Lett. **68**, 2784 (1996).
[57] G. Pozina, J. P. Bergman, B. Monemar, B. Heying, and J. S. Speck, Phys. Status Solidi B **228**, 485 (2001).
[58] S. Hess, F. Walraet, R. A. Taylor, J. F. Ryan, B. Beaumont, and P. Gibart, Phys. Rev. B **58**, R15973 (1998).